

DHGS: Decoupled Hybrid Gaussian Splatting for Driving Scene

Xi Shi^{1*}, Lingli Chen^{1*}, Peng Wei^{1, 2*}, Xi Wu^{1†}, Tian Jiang¹, Yonggang Luo^{1, 2}, Lecheng Xie¹

¹Changan Auto, AILab

²State Key Laboratory of Intelligent Vehicle Safety Technology
{shixi, chenll4, weipeng4, wuxi, jiangtian, luoyg3, xielc}@changan.com.cn

Abstract

Existing Gaussian splatting methods often fall short in achieving satisfactory novel view synthesis in driving scenes, primarily due to the absence of crafty design and geometric constraints for the involved elements. This paper introduces a novel neural rendering method termed Decoupled Hybrid Gaussian Splatting (DHGS), targeting at promoting the rendering quality of novel view synthesis for static driving scenes. The novelty of this work lies in the decoupled and hybrid pixel-level blender for road and non-road layers, without the conventional unified differentiable rendering logic for the entire scene, while still maintaining consistent and continuous superimposition through the proposed depth-ordered hybrid rendering strategy. Additionally, an implicit road representation comprised of a Signed Distance Field (SDF) is trained to supervise the road surface with subtle geometric attributes. Accompanied by the use of auxiliary transmittance loss and consistency loss, novel images with imperceptible boundary and elevated fidelity are ultimately obtained. Substantial experiments on the Waymo dataset prove that DHGS outperforms the state-of-the-art methods. The project page where more video evidences are given is: https://ironbrotherstyle.github.io/dhgs_web.

Introduction

Autonomous Driving (AD) is a data-driven task that appeals the attention of 3D reconstruction community for ages. Due to the expense of collecting a tremendous amount of data, the neural rendering technique which mainly consists of Neural Radiance Fields (NeRFs) (Mildenhall et al. 2020; Barron et al. 2021) and Gaussian Splatting (Kerbl et al. 2023) emerges as an alternative. With the gathered AD data, a synthetic driving scenario can be generated, facilitating close-loop simulation and testing, with a variety of sensor configurations not typically achievable in real-world tests Yang et al. (2023b); Tonderski et al. (2024); Lindström et al. (2024). Compared with NeRF-based approaches, researchers utilizing Gaussian splatting can train and deploy a model more efficiently and flexibly. Despite the significant advancements in scene reconstruction offered by Gaussian

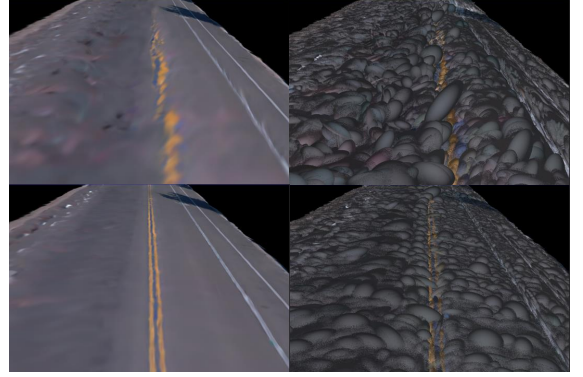


Figure 1: The comparison of rendered road images and ellipsoids on novel view synthesis is presented, with the top row displaying results without SDF regularizer, and the bottom row showcasing results obtained using SDF regularizer. It can be observed that the inclusion of SDF regularization leads the road model to render higher-quality images with the help of enhanced road geometry.

splatting, there are still imperfections in the novel view synthesis capabilities, especially for critical downstream perceptual tasks such as online mapping (Li et al. 2024) of AD scenes. Current methods either model the whole driving scene in a consolidated manner (Kerbl et al. 2023; Huang et al. 2024a; Cheng et al. 2024; Lu et al. 2024), necessitating a uniform growth and pruning strategy for all scene elements, i.e. road, building, and distant views, or model the near scene and far sky (Wu et al. 2023; Miao et al. 2024) dividually. These approaches tend to emphasize the overall or specific distant elements, often overlooking the nearby synthesis quality, which is brittle and significantly impacted by the change of camera perspective. We believe that prioritizing the road is essential, as its geometric properties are fundamental to the success of AD systems.

In this paper, we propose a static neural rendering method named Decoupled Hybrid Gaussian Splatting for Driving Scene (DHGS) to lift the rendering quality of novel view synthesis, particularly for nearby surroundings with fewer flaws and more subtle details. The insight of the method comes from the existing geometric prior that could be utilized to supervise the nearby road elements along with

*These authors contributed equally.

†Corresponding author.

other non-road environments in a fancy pattern. Specifically, we decouple the whole driving scene into a nearby road model and environment model represented by two distinct Gaussian models, considering optimizing the two models based on their geometric characters accordingly. Before that, point clouds are projected and segmented using semantic 2D masks to derive the initial road and environmental point clouds. The road point cloud is used for pre-training the implicit Signed Distance Field (SDF), which serves as the supervision of road training. The training process is conducted via the introduced depth-ordered hybrid rendering strategy by the blender of rendered images of both models, assisted with transmittance loss that regularizes the accumulated transmittance of each componential Gaussian property, as well as consistency loss which bonds the two areas compactly. Besides, we refine the road elements using an SDF loss that is expressly designed for surface regularization, achieving uniform and orderly road Gaussians. To summarize, the contributions of the proposed DHGS are listed as follows:

- We first propose to decouple the driving scene into near road model and other non-road model, enabling the separate optimization of two models and rendering jointly with the designed depth-ordered hybrid rendering.
- We propose an implicit road representation for enhanced guidance of road Gaussians, complemented by transmittance and consistency losses ensuring continuity and consistency.
- Extensive quantitative and qualitative experiments on the popular Waymo dataset demonstrate that DHGS achieves state-of-the-art performance on scene reconstruction and diversified novel free-view synthesis.

Related Works

Neural Radiance Field Representations

NeRF (Mildenhall et al. 2020) has garnered remarkable attention within the neural rendering domain, pioneering the use of a Multi-Layer Perceptron (MLP) to model 3D scenes implicitly. The computationally intensive neural volume rendering and the finite number of sampling points hinder the deployment of NeRF in intricate and expansive driving scenarios. Mip-NeRF (Barron et al. 2021) proposes a more efficient sampling strategy, refining the sampling region from a single ray to a frustum of a viewing cone. Both Mip-NeRF 360 (Barron et al. 2022) and NeRF++ (Zhang et al. 2020) segment the scene into proximal and distal zones, employing warping operations on the latter to handle the unbounded 3D scene. Instant-NGP (Müller et al. 2022) leverages a hash grid for feature storage and streamlines the MLP size to release the computational burden. Plenoxels (Fridovich-Keil et al. 2022) employs sparse grids to reduce storage space and utilize Spherical Harmonics (SH) to represent the appearance. These approaches rely on data from 360-degree object-centric trajectories, while free and long driving scenes draw less attention. F2-NeRF (Wang et al. 2023) proposes a novel space-warping method that supports arbitrary input camera trajectories, enabling the reconstruction

of driving scenes. StreetSurf (Guo et al. 2023) extends prior object-centric neural surface reconstruction techniques to address the unique challenges inherent in unbounded street perspectives, demonstrating promise for a range of subsequent downstream tasks. While advancements in ray marching and enhanced MLPs have been notable, these methods remain a trade-off between rendering fidelity and efficiency, which may restrict their utility in expansive autonomous driving scenarios.

Gaussian Splatting Representations

3DGS (Kerbl et al. 2023) is a seminal work that pioneers the use of 3D Gaussian ellipsoids to explicitly represent a scene and leverages CUDA for parallel rendering, thereby surpassing NeRFs in both rendering quality and efficiency. HUGS, as introduced in (Zhou et al. 2024a), enables real-time rendering of new perspectives, delivering both 2D and 3D semantic data, delivering both 2D and 3D semantic information with remarkable precision. The vanilla 3DGS focuses solely on pixel color consistency, often overlooking the modeling of geometric structures. Consequently, obvious discontinuities such as artifacts and holes appear under novel viewpoints. This discontinuity phenomenon would be more prominent on AD datasets with sparse training views. DRGS (Chung, Oh, and Lee 2024) introduces a dense depth map as geometry guidance to mitigate overfitting. NeuSG (Chen, Li, and Lee 2023) flattens the Gaussian ellipsoid by designing a regularization loss for the scale parameter, and performs consistent joint optimization in combination with the signed distance field. Scaffold GS (Lu et al. 2024) precisely controls the density of the Gaussian ellipsoid by establishing voxel anchors and corresponding offset vectors and learning the various parameters of the Gaussian through a simple multi-layer network. Gaussian Pro (Cheng et al. 2024) considers the planar prior in the scene, explicitly constraining the growth of Gaussians, achieving amendatory rendering and more compact representation. 2DGS (Huang et al. 2024a) presents a highly efficient differentiable 2D Gaussian renderer, enabling perspective-accurate splatting by leveraging 2D surface modeling, demonstrating superiority in geometric reconstruction. Driving Gaussians (Zhou et al. 2024b), Street Gaussians (Yan et al. 2024) and S³ Gaussians (Huang et al. 2024b) all initialize the point cloud collected by LiDAR instead of the point cloud generated by SfM. Leveraging the dense, accurate data from LiDAR, additional supervision, such as the positional constraint, is introduced to the learning process.

As far as we know, Gaussian Splatting works for AD in the literature pay little attention to the capability of novel view synthesis, resulting in low-quality images under significant camera transformations. We aim to address this issue by decoupling the entire scene into road and non-road regions, optimizing each with guidance from hybrid rendering and geometric regularization of Gaussians, achieving more robust and higher-fidelity rendering quality.

Preliminary

3DGS utilizes a set of 3D Gaussians to explicitly represent a scene, achieving high-fidelity rendering quality and fast

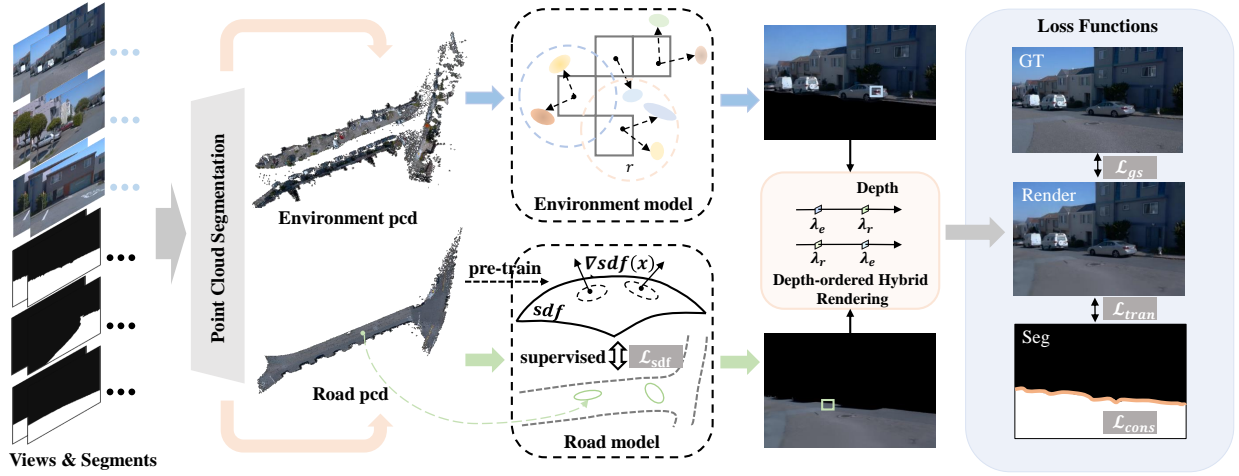


Figure 2: The pipeline of the proposed method for driving scene reconstruction. Given consecutive multi-camera images along with their respective road and non-road masks, we initially generate decoupled road pcd (point cloud) and environment pcd, a road SDF is then pre-trained as subsequent guidance for the road Gaussian model. The Environment pcd enables the initialization for the environment Gaussian model which composes rendered images with images by paratactic road model via the proposed depth-ordered hybrid rendering.

speed via tile-based rasterization. Each Gaussian G is defined as:

$$G(\mathbf{x}) = e^{-\frac{1}{2}(\mathbf{x}-\boldsymbol{\mu})^\top \boldsymbol{\Sigma}^{-1}(\mathbf{x}-\boldsymbol{\mu})}, \quad (1)$$

where $\boldsymbol{\mu}$ is the mean position of Gaussian and \mathbf{x} is a discretional coordinate within the Gaussian space. $\boldsymbol{\Sigma} = RSS^T R^T$, where R is the rotation matrix and S is the scaling matrix. Apart from the spherical harmonic coefficients that represent the anisotropic color of each Gaussian, each pixel color is aggregated by α -blending:

$$\mathbf{c}(\mathbf{x}) = \sum_{i=1}^N c_i \alpha_i \prod_{j=1}^{i-1} (1 - \alpha_j), \quad (2)$$

where α_i is the opacity of the 2D Gaussian projected from 3D Gaussian to the 2D image plane and c_i is the color of the Gaussian in the view direction.

2DGS ensures multi-view consistency well by adopting the expression of surfels and using the projection method specifically for surfels. It achieves 2D Gaussian rendering through ray-splat intersection. The process of ray-splat intersection can be written as:

$$u(\mathbf{x}) = \frac{\mathbf{h}_u^2 \mathbf{h}_v^4 - \mathbf{h}_u^4 \mathbf{h}_v^2}{\mathbf{h}_u^1 \mathbf{h}_v^2 - \mathbf{h}_u^2 \mathbf{h}_v^1}, \quad v(\mathbf{x}) = \frac{\mathbf{h}_u^4 \mathbf{h}_v^1 - \mathbf{h}_u^1 \mathbf{h}_v^4}{\mathbf{h}_u^1 \mathbf{h}_v^2 - \mathbf{h}_u^2 \mathbf{h}_v^1}, \quad (3)$$

where \mathbf{h}_u , \mathbf{h}_v are two planes represented in homogeneous coordinates. By defining the function $G(\mathbf{u}) = \exp\left(-\frac{u^2+v^2}{2}\right)$, and employing the object-space low-pass filter $\hat{G}(\mathbf{x}) = \max\{G(\mathbf{u}(\mathbf{x})), G(\frac{\mathbf{x}-\mathbf{c}}{\sigma})\}$, the rasterization for 2DGS can be shown as:

$$\mathbf{c}(\mathbf{x}) = \sum_{i=1} \mathbf{c}_i \alpha_i \hat{G}_i(\mathbf{u}(\mathbf{x})) \prod_{j=1}^{i-1} (1 - \alpha_j \hat{G}_j(\mathbf{u}(\mathbf{x}))). \quad (4)$$

Method

Overview

The proposed method utilizes initial points clouds and semantic masks as paratactic input of multi-camera views. The pcd (point cloud) initialization phase first generates road and non-road point clouds, which will be further modeled as road and environment Gaussian model. Based on the known road point cloud, we propose to design a mathematical implicit road representation by SDF which serves as a prior for the surface training. The SDF-based surface constraint consists of pre-training and off-line supervision phases, by taking advantage of the distance and normal characters geometrically. We use distinct Gaussians to model road and non-road elements, enhancing the rendering quality during perspective shifts. To achieve that, depth-ordered hybrid rendering is delicately designed, by which the road surface and non-road areas can be coupled and superimposed consistently and continuously, yielding superior performance compared with SOTA methods that employ individual Gaussian model. The rendered image by fusing two models will be supervised by ground truth via Gaussian loss, and optimized in collaboration with the regularization terms. We will sequentially detail this process in the following sections.

Initialization of the Decoupled PCD

Distinguishing ourselves from prior methods, we opt to utilize LiDAR scan which exhibits better multi-view consistency and prior geometric structure compared to the point cloud from SfM. The initial point cloud is classified into road and non-road parts for the subsequent training. As shown in Figure 2, based on the calibrated intrinsic and extrinsic parameters, multi-camera images and their masks generated by Mask2Former (Cheng et al. 2022) are utilized to form colored and semantically labeled single-frame point

clouds. Then we stitch these separate point clouds to build road and environment point clouds.

Pre-trained Surface Based On SDF

To optimize the geometric structure of roads and maintain continuity when facing obvious changes in perspective, we design a road constraint based on surface guidance. Utilizing the segregated road point cloud, we pre-train a signed distance field to represent the road surface implicitly. This approach differs from the joint ray sampling optimization in NeRF and the guidance of geometric structure and image consistency in GSDF (Yu et al. 2024). As road point clouds collected by LiDAR have been calibrated precisely in advance, the excellent geometric structure is suitable to be prior for road learning. A straightforward strategy is directly applying distance constraints to Gaussians that belong to the road. Whereas, considering the spatial geometric characteristics of ellipsoids, imposing constraints only on the centers of Gaussian ellipsoids cannot fully restore their correct geometric shapes, potentially restricting the Gaussian distribution to some extent. We therefore adopt a pre-trained model to optimize the Gaussian distribution by adjusting Gaussian parameters nearing the road surface. To this end, we design specific regularization terms for road-related Gaussians. These include distance and normal direction constraints that ensure Gaussians stay close to the road surface and align with the normal direction of the road surface concurrently.

We utilize a predefined network $f_\theta(x)$ for predicting the corresponding SDF value given the positional coordinate of the point cloud. Data normalization is imposed on all the training and testing coordinates to ensure stability and enhanced performance. To equalize the number of points on and off the isosurface, we define the road point cloud as \mathcal{P}_r , and assign a hypothetical SDF value of zero to each point $x_p \in \mathcal{P}_r$ on the isosurface. For points off the isosurface, we establish a proximity range around each point in \mathcal{P}_r , perform random sampling within this range to obtain sample points $\mathcal{P}_s \supset \mathcal{P}_r$, for $\forall x_s \in \mathcal{P}_s$, we build a map from point x_s to the signed euclidean distance d_s as:

$$d_s = \text{sgn}(x_s^{(3)} - x_r^{s(3)}) \cdot \|x_s - x_r^s\|_2, \quad (5)$$

where x_r^s is the nearest point of x_s in \mathcal{P}_r . Considering that bumps exist in uneven road surfaces, we generate the normal direction for each point in \mathcal{P}_r to assist in the training of the SDF. To be specific, for $\forall x_r \in \mathcal{P}_r$, set X_r as k -nearest neighbors of x_r , by performing SVD:

$$U\Lambda V^T = \text{svd}(\tilde{X}), \quad (6)$$

where $\tilde{X} \triangleq X_r - \bar{X}_r$. The right singular vector v_i corresponding to the minimum singular value λ_i is finally regarded as the normal of x_r , noted as n_r .

We supervise the predicted SDF value from the network with our pre-computed ground truth by incorporating a newly proposed normal loss based on the predicted normal

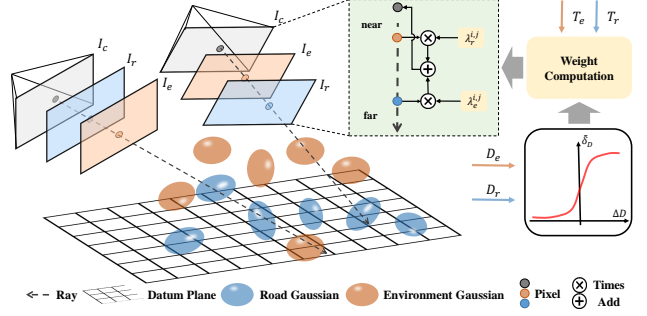


Figure 3: The diagram illustrates the proposed depth-ordered hybrid rendering strategy for the environment and road model. Corresponding primitives of each model generate pixels with colors independently through Gaussian splatting. These colors are then composited based on their rendered depths and transmittances, producing the final rendered image.

direction. The optimization goal of road SDF is written as:

$$\begin{aligned} \min_{\theta} \{L(\theta) := & \frac{1}{|\mathcal{P}_s|} \sum_{x_s \in \mathcal{P}_s} \|f_\theta(\tilde{x}_s) - d_s\|_2^2 \\ & + \frac{1}{|\mathcal{P}_r|} \sum_{x_r \in \mathcal{P}_r} \{\lambda_n \sin^2 \langle \nabla f_\theta(\tilde{x}_r), n_r \rangle \\ & + \lambda_{\text{eik}} (\|\nabla f_\theta(\tilde{x}_r)\|_2 - 1)^2\}, \end{aligned} \quad (7)$$

in which the first and last terms refer to SDF value regularization and eikonal regularizer respectively, the middle term represents normal loss, and $|\cdot|$ refers to the number of points in the point cloud. The optimal parameters $\theta^* = \arg \min_{\theta} L(\theta)$ will be frozen and used to guide the learning of road Gaussians in the following processes.

Depth-Ordered Hybrid Rendering

Based on the predefined initial semantic non-road point cloud \mathcal{P}_e and road point cloud \mathcal{P}_r , we build the environment model and road model simultaneously. In this paper, Scaffold GS and 2DGS are chosen as the fundamental Gaussian splatting substrates. By executing forward rendering separately, output images I_e and I_r , as well as depth maps and accumulated transmittance maps will be generated in parallel. In our experiments, simply fusing I_e and I_r linearly causes inferior image quality. The reason is that naive fusion degrades the learning of Gaussian properties without the solicitude for real depth relationship of Gaussians from the environment and road model. The depth D is rendered based on d_i that indicates each splat from the camera, following the rasterization pipeline in (Dai et al. 2024; Chung, Oh, and Lee 2024),

$$D = \sum_{i=1}^N d_i \alpha_i \prod_{j=1}^{i-1} (1 - \alpha_j), T = \prod_{i=1}^N (1 - \alpha_i).$$

Accordingly, we adopt a pixel-level hybrid rendering method based on depth sorting, as depicted in Figure 3. Assuming that the tuple $[I_e, D_e, T_e]$ severally represents image,

Metrics	Scene Reconstruction			Novel View Synthesis			Free-view Novel View Synthesis			
	PSNR \uparrow	SSIM \uparrow	LPIPS \downarrow	PSNR \uparrow	SSIM \uparrow	LPIPS \downarrow	FID \downarrow			
							Set1	Set2	Set3	Set4
3DGS	26.91	0.8295	0.3101	25.92	0.8089	0.3218	53.12	61.93	82.52	61.53
2DGS	24.75	0.7919	0.3746	24.26	0.7819	0.3798	101.9	105.5	123.4	105.6
Gaussian Pro	25.90	0.8019	0.3250	25.09	0.7827	0.3358	60.52	68.75	90.12	69.05
Scaffold GS	<u>28.04</u>	<u>0.8428</u>	<u>0.3039</u>	26.87	0.8224	<u>0.3142</u>	<u>51.93</u>	<u>58.25</u>	<u>78.64</u>	<u>57.85</u>
Ours	28.09	0.8460	0.2960	<u>26.77</u>	<u>0.8216</u>	0.3100	48.05	56.93	75.72	55.52

Table 1: The quantitative comparison between our method with four SOTA works on PSNR, SSIM, LPIPS, and FID metrics computed over all clips on the Waymo dataset. We adopt the same training data for each method and follow the corresponding experimental settings strictly. The best and second best are marked in **bold** and underlined for each metric respectively.

depth, and accumulated transmittance rendered by the environment model, $[I_r, D_r, T_r]$ indicates image, depth, and accumulated transmittance rendered by the road model in the same manner. The composite rendering strategy is presented as:

$$I_c = \lambda_r I_r + \lambda_e I_e, \quad (8)$$

where λ_r and λ_e are the weights for fusing I_r and I_e rendered from the environment model and road model respectively, which are organized as:

$$\begin{aligned} \lambda_r &= T_e \delta_D + (1 - \delta_D), \\ \lambda_e &= T_r (1 - \delta_D) + \delta_D, \end{aligned} \quad (9)$$

where δ_D is the item for composing weights of fusion, which is defined as:

$$\delta_D = \begin{cases} 1 & D_r > D_e \\ 0 & D_r \leq D_e \end{cases} \quad (10)$$

One limitation of blending the rendered images discontinuously is that the weights also vary discretely, which will result in the distinct appearance of boundary lines on the edge of road and non-road regions. We thus introduce a consecutive strategy to model the dynamic weights based on the rendered depth. Concretely, the sigmoid function $S(x)$ is utilized to realize the ordered rendering as:

$$S(x) = \frac{1}{1 + \exp(-s_\sigma x)}, \quad (11)$$

where s_σ is a given hyperparameter. We set $\Delta D = D_r - D_e$ indicating depth difference as the input of $S(x)$ to obtain $\tilde{\delta}_D = S(\Delta D)$, the smoother weights can be shown as:

$$\begin{aligned} \lambda_r &= T_e \tilde{\delta}_D + (1 - \tilde{\delta}_D), \\ \lambda_e &= T_r (1 - \tilde{\delta}_D) + \tilde{\delta}_D. \end{aligned} \quad (12)$$

With the proposed smooth rendering mechanism, the overall rendering quality can be significantly improved and the synthesis of new perspectives will appear more natural and fluid.

Loss Functions

The overall training objective is given as follows:

$$\mathcal{L} = \mathcal{L}_{gs} + \lambda_{tran} \mathcal{L}_{tran} + \lambda_{sdf} \mathcal{L}_{sdf} + \lambda_{cons} \mathcal{L}_{cons} + \lambda_{tv} \mathcal{L}_{tv}, \quad (13)$$

among which \mathcal{L}_{gs} is responsible for measuring the reconstruction discrepancy used in 3DGS:

$$\mathcal{L}_{gs} = \lambda \mathcal{L}_1(I_c, I_{gt}) + (1 - \lambda) \mathcal{L}_{D-SSIM}(I_c, I_{gt}), \quad (14)$$

where I_{gt} is the ground truth. The \mathcal{L}_{sdf} consists of two parts, distance loss and normal loss of the road surface, written as:

$$\mathcal{L}_{sdf} = \frac{1}{N} \sum_{i=1}^N \{ \lambda_d \|f_{\theta^*}(\tilde{x}_i)\|_1 + \lambda_n \sin^2 \langle \nabla f_{\theta^*}(\tilde{x}_i), t_n \rangle \}, \quad (15)$$

where $t_n = t_u \times t_v$ refers to 2D primitive normal of Gaussian. \mathcal{L}_{tran} supervises the accumulated transmittance of road and non-road regions, ensuring their consistency with the corresponding regions in the 2D semantic segmentation, which is represented as:

$$\mathcal{L}_{tran} = \frac{1}{|M|} (\|T_e - M\|_F^2 + \|T_r - (1 - M)\|_F^2), \quad (16)$$

where M refers to the semantic mask of the image, $|\cdot|$ denotes the total number of pixels for given matrix. The \mathcal{L}_c enforces consistency between the depth rendered by environment Gaussians and road Gaussians:

$$\mathcal{L}_{cons} = \max_j \min_i |D_e^{i,j} - D_r^{i,j}|, \quad (17)$$

where i and j satisfying $\tilde{M}^{i,j} \neq 0$, \tilde{M} refers to the banded boundary generated by binary mask M , and the orange band at the bottom right corner of Figure 2 intuitively shows the distribution of elements in \tilde{M} . We follow Plenoxels (Fridovich-Keil et al. 2022) and use a total variation loss \mathcal{L}_{tv} . The collective impact of the aforementioned loss functions enables DHGS to generate high-quality renderings that preserve a continuous geometric structure.

Experiments and Analysis

Experimental Settings

Datasets and Metrics. We experiment on the publicly available urban scene datasets Waymo (Sun et al. 2020), 32 static



Figure 4: Comparison of different methods on the Waymo dataset, the left column and right column display the quality of scene reconstruction and novel view synthesis respectively. Our method achieves high-quality reconstruction for both the environment region and the road areas, excelling over other comparative methods in these aspects.

scenes are adopted as the same as EmerNeRF (Yang et al. 2023a). We employ multiple metrics to evaluate the performance of the proposed method and baselines. PSNR, SSIM, and LPIPS metrics are utilized to validate the quality of rendered images with ground truth. For novel views without ground truth, we introduce FID (Heusel et al. 2017) to evaluate the image quality. The averaged metrics across all clips are calculated as comparative values.

Baselines. We compare our method with state-of-the-art and publicly available works. 3DGS (Kerbl et al. 2023), 2DGS (Huang et al. 2024a), Gaussian Pro (Cheng et al. 2024), and Scaffold GS (Lu et al. 2024) are chosen as the comparison methods having been regarded for their outstanding performances.

Implementation details. The initial point cloud is randomly downsampled to 600,000 points. All methods are trained for 60,000 iterations. For the pre-trained SDF network, we employ an 8-layer MLP and train it for 20,000 iterations. The normals of surface points are computed using SVD with 50 neighbors, and the weights for the normal loss and the eikonal loss of the SDF network are set to 0.1 and 0.01. The weights λ_{tran} , λ_{sdf} , λ_{cons} , λ_{tv} , λ_d and λ_n of the overall training loss are set to 0.1, 1.0, 0.04, 0.1, 0.1 and 0.1. We set the densification intervals for the Gaussian ellipsoids in

the environment model and road model to 200 and 300 respectively. The learning rate for the anchor position in the environment model is set as 0.00016, the remaining learning rates are kept consistent with the original settings. For each clip, we utilize all the front, left-front, and right-front views of the entire sequence for training, with a 4:1 split ratio between the training and testing sets. The training set is referred to as the reconstruction views, while the testing set is called the novel views. We further apply unrestricted transformations on camera poses to validate the potential of the model on data-driven simulation, which is referred to as free-view novel view synthesis.

Comparisons

We benchmark our method against established baselines in scene reconstruction, novel view synthesis, and free-view reconstruction novel view synthesis that stands for notable viewpoints transfer. All methods employ a consistent set of reconstruction views for training, while the remainder are employed as novel views for testing in each clip. The qualitative and quantitative results will be examined in the subsequent sections, with an ablation study included for analysis.

Scene Reconstruction on the Waymo Dataset. For reconstruction views, we calculate the mean PSNR, SSIM, and

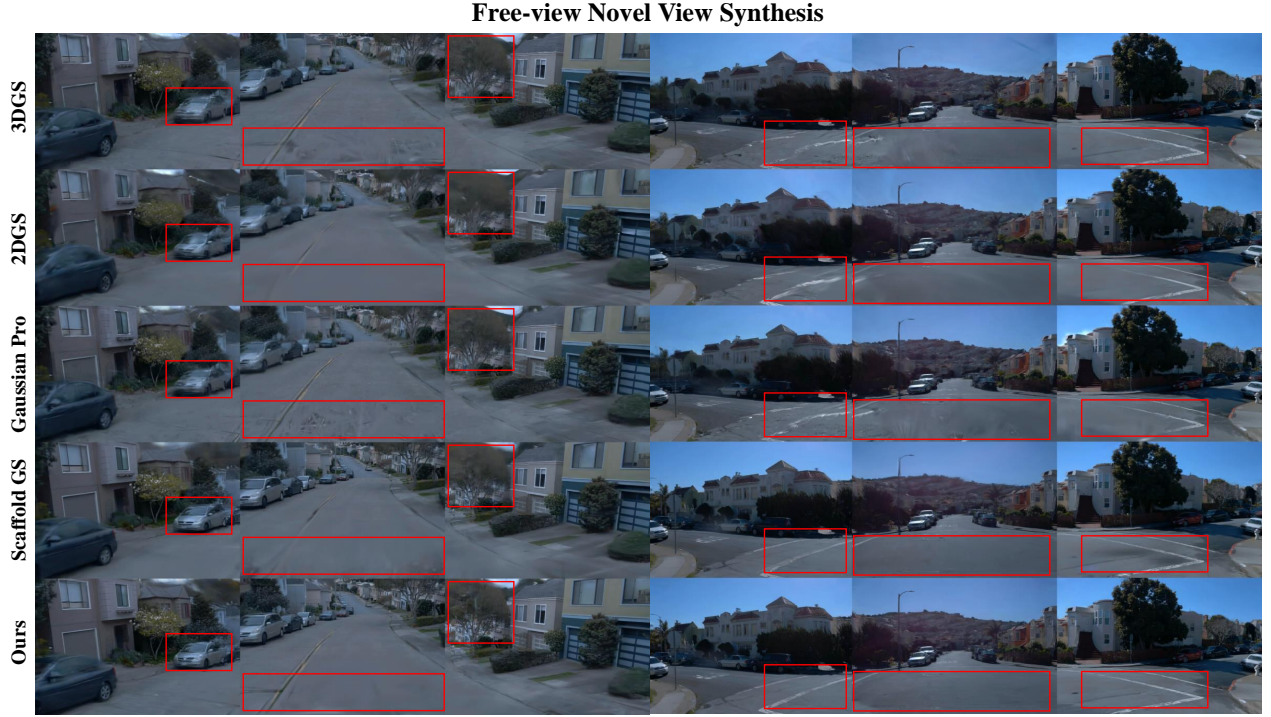


Figure 5: Visual comparisons on the free-view novel view synthesis. The left and right columns respectively exhibit the results of *Set3* and *Set4* under the free viewpoint setting, where our method significantly outperforms other comparative methods in capturing both road and environment details.

LPIPS of the rendered images across 32 clips, as shown in Table 1. Our method outperforms all the mainstream methods: including 3DGS, 2DGS, Gaussian Pro, and Scaffold GS. The left part of Figure 4 displays the rendered images of the reconstruction views from our method and its competitors. It can be noticed that our method achieves better reconstruction quality with finer details than competitive methods, from which the road area rendered by our method contains richer texture information.

Novel View Synthesis on the Waymo dataset. We assess the aforementioned methods on the novel views. Table 1 illustrates the validation results, demonstrating that our method surpasses most rival methods, such as 3DGS, 2DGS, and Gaussian Pro, and achieves comparable results to Scaffold GS. Notably, Scaffold GS achieves the best performance in terms of PSNR and SSIM. As depicted in the right part of Figure 4, blurriness appears in some non-road areas (highlighted by red boxes) for 3DGS, 2DGS, and Gaussian Pro. In contrast, our method restores more road details (lane lines within the red boxes) thanks to the imposition of geometric constraints on the road, whereas other methods such as 2DGS, Gaussian Pro, and Scaffold GS fail to preserve these subtleties. Despite novel views not being part of the training set, their camera poses variations are minimal compared to trained views, which can be simply concluded as the interpolation of trained views. Such minor variations in novel views do not sufficiently reflect the geometric representation capability of the model.

Free-view Novel View Synthesis on the Waymo dataset.

To further underscore the geometric consistency of our approach, we evaluate the trained model on free-view novel views with more pronounced camera pose variations. We adjust the poses of the cameras relative to the vehicle, mimicking various observation perspectives for different vehicle types with diverse camera positions. In this paper, we outline four types of transformations to the camera poses, with detailed configurations provided in the supplementary material. Given the absence of ground truth for these novel views, we adopt the FID metric, adept at gauging the feature discrepancy between the original input views and the free-view novel views. The comparisons of FID for free-view novel views are also presented in Table 1, where our method achieves the highest performance compared to other methods in all four configurations with a significant margin of superiority. The qualitative rendering results, depicted in Figure 5, reveal that free-view rendered images produced by other methods suffer from extensive artifacts and lane line breakage. In contrast, our method consistently captures environmental and road details, including lane lines, even amidst substantial camera pose shifts. The results further validate that the regularization constraints and the depth-ordered hybrid rendering strategy we proposed facilitate the acquisition of an optimal geometric structure, thereby showcasing the robustness of our approach in free-view novel view synthesis. More visual comparisons can be found in supplemental materials.



Figure 6: Qualitative comparison for free-view novel views of ablation studies. The emphasized patches reveal that these regularization terms contribute to the accurate reconstruction of road geometry.

Ablation Study.

To assess the efficacy of our proposed regularization components, we perform an ablation study, systematically omitting the SDF, transmittance, and consistency losses, denoted as "w/o SDF", "w/o tran", and "w/o cons". The quantitative results for scene reconstruction, novel view synthesis, and free-view novel view synthesis are consolidated in Table 2. For scene reconstruction and novel view synthesis, the absence of the SDF loss leads to a decline in performance metrics, whereas the exclusion of transmittance loss or consistency loss has a minimal impact. Conversely, for free-view novel view synthesis, the removal of any loss escalates the FID score, signifying a greater divergence between the novel views and the originals. To more intuitively illustrate the specific contributions of these components, we present the visualization results of free-view novel views synthesis in Figure 6. Specifically, the SDF loss ensures the fidelity of road geometry, the consistency loss guarantees a seamless connection between the environment model and the road model. The transmittance loss ensures precise alignment of the rendering areas of both models with the 2D segmentation, thus averting rendering artifacts. Therefore, each regularization term is integral to our DHGS framework.

Conclusions

In this paper, we propose a novel reconstruction method called DHGS, which aims to elevate the rendering quality of novel view synthesis for static driving scenes. DHGS leverages two decoupled models to represent the road and environment separately, which are then merged via a pixel-level hybrid renderer, facilitated by our innovative depth-ordered hybrid rendering strategy. Additionally, consistency loss and transmittance loss are proposed to constrain the basal models, allowing for the generation of continuous and consistent rendered images. Moreover, we develop a road surface regularization term grounded in SDF to ensure better geometric consistency of the road surface, guaranteeing stable image quality as perspective changes drastically. Through

<i>Metrics</i>	w/o SDF	w/o tran	w/o cons	Ours
<i>Scene Reconstruction</i>				
PSNR \uparrow	27.76	28.18	28.01	28.09
SSIM \uparrow	0.8381	0.8473	0.8453	0.8460
LPIPS \downarrow	0.3147	0.2934	0.3007	0.2961
<i>Novel View Synthesis</i>				
PSNR \uparrow	26.29	26.63	26.68	26.77
SSIM \uparrow	0.8151	0.8213	0.8205	0.8217
LPIPS \downarrow	0.3195	0.3113	0.3154	0.3100
<i>Free-view Novel View Synthesis</i>				
FID \downarrow	61.16	61.02	62.49	59.06

Table 2: Quantitative results of ablation experiments on the Waymo dataset, with each metric averaged across all clips.

extensive testing on the Waymo dataset, our method reveals the state-of-the-art performance in both reconstruction and novel view synthesis of our method.

Acknowledgments

This work would thank Bo Zheng and Fan Jin for providing the necessary help in the preparation of training data.

References

- Barron, J. T.; Mildenhall, B.; Tancik, M.; Hedman, P.; Martin-Brualla, R.; and Srinivasan, P. P. 2021. Mip-nerf: A multiscale representation for anti-aliasing neural radiance fields. In *Proceedings of the IEEE/CVF International Conference on Computer Vision (ICCV)*, 5855–5864.
- Barron, J. T.; Mildenhall, B.; Verbin, D.; Srinivasan, P. P.; and Hedman, P. 2022. Mip-nerf 360: Unbounded anti-aliased neural radiance fields. In *Proceedings of the IEEE/CVF Conference on Computer Vision and Pattern Recognition (CVPR)*, 5470–5479.
- Chen, H.; Li, C.; and Lee, G. H. 2023. Neusg: Neural implicit surface reconstruction with 3d gaussian splatting guidance. *arXiv preprint arXiv:2312.00846*.
- Cheng, B.; Misra, I.; Schwing, A. G.; Kirillov, A.; and Girdhar, R. 2022. Masked-attention mask transformer for universal image segmentation. In *Proceedings of the IEEE/CVF Conference on Computer Vision and Pattern recognition (CVPR)*, 1290–1299.
- Cheng, K.; Long, X.; Yang, K.; Yao, Y.; Yin, W.; Ma, Y.; Wang, W.; and Chen, X. 2024. Gaussianpro: 3d gaussian splatting with progressive propagation. *arXiv preprint arXiv:2402.14650*.
- Chung, J.; Oh, J.; and Lee, K. M. 2024. Depth-regularized optimization for 3d gaussian splatting in few-shot images. In *Proceedings of the IEEE/CVF Conference on Computer Vision and Pattern Recognition (CVPR)*, 811–820.

- Dai, P.; Xu, J.; Xie, W.; Liu, X.; Wang, H.; and Xu, W. 2024. High-quality surface reconstruction using gaussian surfels. *arXiv preprint arXiv:2404.17774*.
- Fridovich-Keil, S.; Yu, A.; Tancik, M.; Chen, Q.; Recht, B.; and Kanazawa, A. 2022. Plenoxels: Radiance fields without neural networks. In *Proceedings of the IEEE/CVF Conference on Computer Vision and Pattern Recognition (CVPR)*, 5501–5510.
- Guo, J.; Deng, N.; Li, X.; Bai, Y.; Shi, B.; Wang, C.; Ding, C.; Wang, D.; and Li, Y. 2023. Streetsurf: Extending multi-view implicit surface reconstruction to street views. *arXiv preprint arXiv:2306.04988*.
- Heusel, M.; Ramsauer, H.; Unterthiner, T.; Nessler, B.; and Hochreiter, S. 2017. Gans trained by a two time-scale update rule converge to a local nash equilibrium. *Advances in Neural Information Processing Systems (NIPS)* 30.
- Huang, B.; Yu, Z.; Chen, A.; Geiger, A.; and Gao, S. 2024a. 2d gaussian splatting for geometrically accurate radiance fields. *arXiv preprint arXiv:2403.17888*.
- Huang, N.; Wei, X.; Zheng, W.; An, P.; Lu, M.; Zhan, W.; Tomizuka, M.; Keutzer, K.; and Zhang, S. 2024b. S³ gaussian: Self-supervised street gaussians for autonomous driving. *arXiv preprint arXiv:2405.20323*.
- Kerbl, B.; Kopanas, G.; Leimkühler, T.; and Drettakis, G. 2023. 3d gaussian splatting for real-time radiance field rendering. *ACM Transactions on Graphics (TOG)* 42(4):1–14.
- Li, T.; Jia, P.; Wang, B.; Chen, L.; Jiang, K.; Yan, J.; and Li, H. 2024. Laneseqnet: Map learning with lane segment perception for autonomous driving. In *Proceedings of the International Conference on Learning Representations (ICLR)*.
- Lindström, C.; Hess, G.; Lilja, A.; Fatemi, M.; Hammarstrand, L.; Petersson, C.; and Svensson, L. 2024. Are nerfs ready for autonomous driving? towards closing the real-to-simulation gap. In *Proceedings of the IEEE/CVF Conference on Computer Vision and Pattern Recognition (CVPR)*, 4461–4471.
- Lu, T.; Yu, M.; Xu, L.; Xiangli, Y.; Wang, L.; Lin, D.; and Dai, B. 2024. Scaffold-gs: Structured 3d gaussians for view-adaptive rendering. In *Proceedings of the IEEE/CVF Conference on Computer Vision and Pattern Recognition (CVPR)*, 20654–20664.
- Miao, S.; Huang, J.; Bai, D.; Qiu, W.; Liu, B.; Geiger, A.; and Liao, Y. 2024. Edus: Efficient depth-guided urban view synthesis. In *European Conference on Computer Vision (ECCV)*.
- Mildenhall, B.; Srinivasan, P.; Tancik, M.; Barron, J.; Ramamoorthi, R.; and Ng, R. 2020. Nerf: Representing scenes as neural radiance fields for view synthesis. In *European Conference on Computer Vision (ECCV)*.
- Müller, T.; Evans, A.; Schied, C.; and Keller, A. 2022. Instant neural graphics primitives with a multiresolution hash encoding. *ACM Transactions on Graphics (TOG)* 41(4):1–15.
- Rudin, L. I., and Osher, S. 1994. Total variation based image restoration with free local constraints. In *Proceedings of 1st International Conference on Image Processing (ICIP)*, volume 1, 31–35. IEEE.
- Sun, P.; Kretschmar, H.; Dotiwalla, X.; Chouard, A.; Patnaik, V.; Tsui, P.; Guo, J.; Zhou, Y.; Chai, Y.; Caine, B.; et al. 2020. Scalability in perception for autonomous driving: Waymo open dataset. In *Proceedings of the IEEE/CVF Conference on Computer Vision and Pattern Recognition (CVPR)*, 2446–2454.
- Tonderski, A.; Lindström, C.; Hess, G.; Ljungbergh, W.; Svensson, L.; and Petersson, C. 2024. Neurad: Neural rendering for autonomous driving. In *Proceedings of the IEEE/CVF Conference on Computer Vision and Pattern Recognition (CVPR)*, 14895–14904.
- Wang, P.; Liu, Y.; Chen, Z.; Liu, L.; Liu, Z.; Komura, T.; Theobalt, C.; and Wang, W. 2023. F2-nerf: Fast neural radiance field training with free camera trajectories. In *Proceedings of the IEEE/CVF Conference on Computer Vision and Pattern Recognition (CVPR)*, 4150–4159.
- Wu, Z.; Liu, T.; Luo, L.; Zhong, Z.; Chen, J.; Xiao, H.; Hou, C.; Lou, H.; Chen, Y.; Yang, R.; et al. 2023. Mars: An instance-aware, modular and realistic simulator for autonomous driving. In *CAAI International Conference on Artificial Intelligence*, 3–15. Springer.
- Yan, Y.; Lin, H.; Zhou, C.; Wang, W.; Sun, H.; Zhan, K.; Lang, X.; Zhou, X.; and Peng, S. 2024. Street gaussians for modeling dynamic urban scenes. *arXiv preprint arXiv:2401.01339*.
- Yang, J.; Ivanovic, B.; Litany, O.; Weng, X.; Kim, S. W.; Li, B.; Che, T.; Xu, D.; Fidler, S.; Pavone, M.; et al. 2023a. Emernerf: Emergent spatial-temporal scene decomposition via self-supervision. *arXiv preprint arXiv:2311.02077*.
- Yang, Z.; Chen, Y.; Wang, J.; Manivasagam, S.; Ma, W.-C.; Yang, A. J.; and Urtasun, R. 2023b. Unisim: A neural closed-loop sensor simulator. In *Proceedings of the IEEE/CVF Conference on Computer Vision and Pattern Recognition (CVPR)*, 1389–1399.
- Yu, M.; Lu, T.; Xu, L.; Jiang, L.; Xiangli, Y.; and Dai, B. 2024. Gsdf: 3dgs meets sdf for improved rendering and reconstruction. *arXiv preprint arXiv:2403.16964*.
- Zhang, K.; Riegler, G.; Snavely, N.; and Koltun, V. 2020. Nerf++: Analyzing and improving neural radiance fields. *arXiv preprint arXiv:2010.07492*.
- Zhou, H.; Shao, J.; Xu, L.; Bai, D.; Qiu, W.; Liu, B.; Wang, Y.; Geiger, A.; and Liao, Y. 2024a. Hugs: Holistic urban 3d scene understanding via gaussian splatting. In *Proceedings of the IEEE/CVF Conference on Computer Vision and Pattern Recognition (CVPR)*, 21336–21345.
- Zhou, X.; Lin, Z.; Shan, X.; Wang, Y.; Sun, D.; and Yang, M.-H. 2024b. Drivinggaussian: Composite gaussian splatting for surrounding dynamic autonomous driving scenes. In *Proceedings of the IEEE/CVF Conference on Computer Vision and Pattern Recognition (CVPR)*, 21634–21643.

Supplemental Material for DHGS: Decoupled Hybrid Gaussian Splatting for Driving Scene

In the supplementary material, we introduce more details on the method and implementation in Sec. A. Extra experimental results are illustrated in Sec. B.

A. Implementation Details

Initial PCD with sky sphere. To deal with the floaters phenomenon in new perspectives, we devise a straightforward yet effective strategy. We construct a hemispherical virtual sky point cloud layer that envelops the LiDAR point clouds. The radius and center of this sky point cloud are determined by the scale and the average distribution of the LiDAR points, ensuring an accurate representation of the sky’s spatial characteristics. Additionally, we apply appropriate coloring to the sky point cloud to maintain its visual integrity, as depicted in Figure A1. Table A1 presents a comparative analysis between incorporating the sky sphere point cloud into 3DGS and not incorporating it. It is evident that the introduction of sky sphere pcd is able to improve the rendering quality, no matter in reconstruction or novel view synthesis. For fairness, we integrate this sky sphere point cloud mechanism into all comparative methods, such that the potential biases stemming from differences in sky handling can be eliminated.

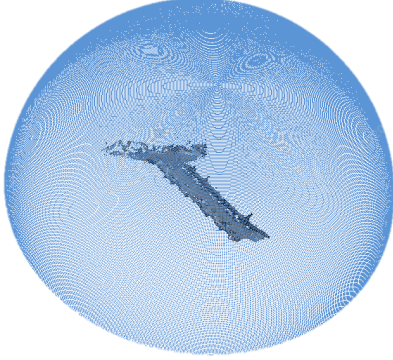


Figure A1: Visualization of incorporating a sky sphere point cloud into the initial point cloud.

Initial PCD	PSNR \uparrow	SSIM \uparrow	LPIPS \downarrow	FID \downarrow
PCD wo sky sphere	25.63	0.8062	0.3265	67.52
PCD wi sky sphere	25.92	0.8089	0.3218	64.77

Table A1: The quantitative results of 3DGS with and without incorporating the sky sphere point cloud into the initial point cloud. The FID here is averaged on FIDS of all four sets.

Sigmoid distance constraint. In addition to optimizing the road model, we also utilize a distance constraint mechanism for the environmental model. Rather than directly applying distance regularization to the offsets, we adopt a more

restrictive approach, overlaying a sigmoid function on the offsets. This achieves effective boundary control over the offsets. Specifically, we implement the transformation using the following formula:

$$\mu_k = x_v + \lambda_\sigma \cdot (2 \cdot \text{sigmoid}(\mathcal{O}_v \cdot l_v) - 1),$$

where x_v refers to the coordinate of the anchor point, μ_k refers to the center coordinates of the k -th neural Gaussian corresponding to the anchor. l_v and \mathcal{O}_v represent scaling factor and offset vector respectively. This design ensures that the offsets are strictly confined within a reasonable and finite range, thereby preventing the generation of neural Gaussian ellipsoids that are excessively distant from their anchor points. Consequently, the power of the environmental model to represent fine details is significantly enhanced.

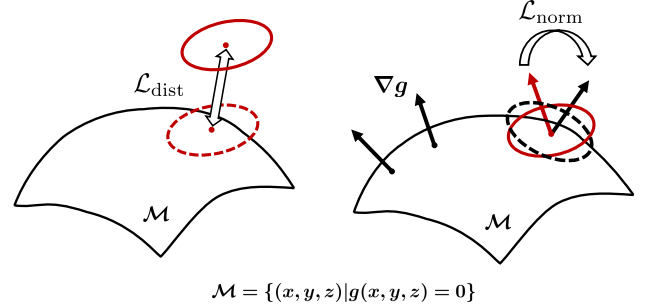


Figure A2: The simplified sketch of the SDF regularizer, where $\mathcal{L}_{\text{dist}}$ and $\mathcal{L}_{\text{norm}}$ refer to the distance constraint and normal constraint guided by the zero-level set of SDF, the function g refers to the ideal pretrained SDF.

Regularization loss. The total variation regularization \mathcal{L}_{tv} (Rudin and Osher 1994) is applied in this study to refine the rendered pixel depths. The depth map can be generated through a rendering process similar to the one we calculate color: $D = \lambda_r D_r + \lambda_e D_e$, to maintain the continuity of D near boundaries of two depth maps, the TV regularizer can be represented as:

$$\mathcal{L}_{\text{tv}} = \sum_{\tilde{M}^{i,j} \neq 0} ((D^{i,j-1} - D^{i,j})^2 + (D^{i+1,j} - D^{i,j})^2)^{\frac{1}{2}}.$$

The SDF regularizer \mathcal{L}_{sdf} , inspired by NeuSG originally optimizing the positions and orientations of 3D Gaussians, is applied in this paper similarly to 2D Gaussians. Specifically, we leverage the gradient direction of the pre-trained SDF to guide the orientation updates of the 2D Gaussians, while simultaneously constraining their disk centers to align with the SDF. This approach guarantees a seamless integration which is intuitively illustrated in Figure A2.

B. Experimental results

Free-view Novel View Synthesis Settings. We apply four transformations to the pose of the camera relative to the vehicle, including rotations and translations. The motive is that transferring the visual data from the collecting vehicle to a new vehicle with a diverse sensor setup is frequently demanded in AD. We set four settings based on the camera

Setting	front-left		front		front-right	
	<i>Translation</i>	<i>Rotation</i>	<i>Translation</i>	<i>Rotation</i>	<i>Translation</i>	<i>Rotation</i>
<i>Set1</i>	(0.5, 0.5, 0)	(0, 0, 0)	(1, 0, 0)	(0, 0, 0)	(0.5, -0.5, 0)	(0, 0, 0)
<i>Set2</i>	(0.5, 0.5, -0.5)	(0, 0, 0)	(1, 0, 0)	(0, 0, 0)	(0.5, -0.5, -0.5)	(0, 0, 0)
<i>Set3</i>	(0.5, 0.5, -0.5)	(10, 0, 0)	(1, 0, 0)	(0, -10, 0)	(0.5, -0.5, -0.5)	(-10, 0, 0)
<i>Set4</i>	(0, 1, 0)	(0, 0, 0)	(0, 1, 0)	(0, 0, 0)	(0, 1, 0)	(0, 0, 0)

Table A2: The table illustrates four different parameter settings for free-view novel view synthesis, where *Translation* refers to the translation component, *Rotation* refers to the rotation component, the corresponding three numbers are the lengths of translation in meter, and the magnitudes of three Euler angles for rotation in degree.

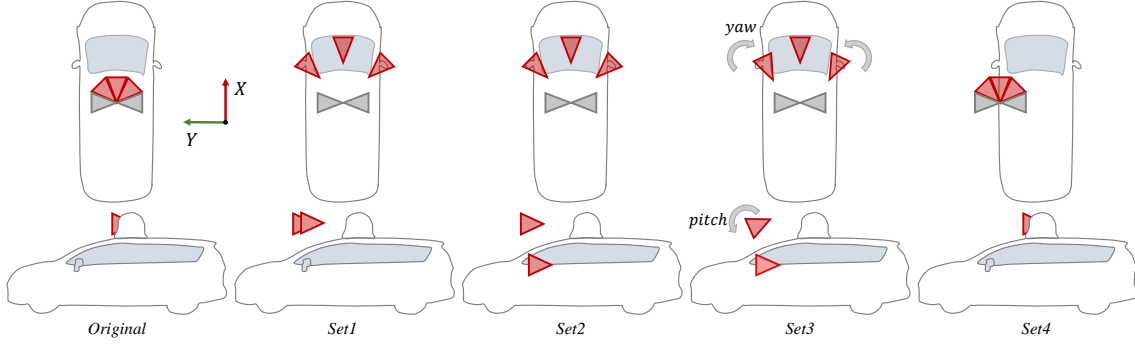


Figure A3: The camera layouts after applying the four settings of camera pose. The top row represents the camera layouts after applying various camera pose settings from a bird's eye view, while the bottom row shows the same transformations from a side view.

positions of the Waymo dataset to simulate the camera displacements caused by changes in vehicle type. The detailed variation amplitudes for the front, front-left, and front-right camera under each transformation are outlined in Table A2, where *Translation* denotes the translation distances of the camera along the x , y , and z axes in meter, and *Rotation* represents the rotation angles around the *yaw*, *pitch*, and *roll* axes in degree. Figure A3 depicts the differences in the four transformed camera poses compared to the original Waymo configuration.

The qualitative result on the Waymo dataset. In addition to the quantitative metrics and qualitative rendered images elaborated in the main document, we attach additional qualitative results to provide a more intuitive performance evaluation of each method. As shown in Figures A5, A6, and A7, the qualitative results indicate that our method achieves the best visual quality in the modeling of both environmental backgrounds and road structures, demonstrating superior capability in scene reconstruction, novel view synthesis, and free-view novel view synthesis.

Comparative analysis of the compound mode of Gaussians. We compare several distinct assembly ways of road and non-road models, as detailed in Table A3. Figure A4 illustrates qualitative comparisons of three compound modes. It can be concluded that leveraging Scaffold GS and 2DGS to represent the environment and road model severally harvests optimal performance. Benefiting from the robustness



Figure A4: Qualitative comparisons of different compound modes on the Waymo dataset, with top ($E_{3DGS} + R_{3DGS}$), middle ($E_{ScaffoldGS} + R_{3DGS}$), and bottom ($E_{ScaffoldGS} + R_{2DGS}$). The highlighted regions demonstrate that our method achieves the best rendering quality.

of Scaffold GS in changing views and the inherent superiority of flat 2DGS representing the road surface, DHGS achieves superior rendering results both in the road and environment areas, exhibiting fewer floaters on the road and capturing finer environmental details..

Compound Mode	PSNR \uparrow		FID \downarrow			
	<i>Train</i>	<i>Test</i>	<i>Set1</i>	<i>Set2</i>	<i>Set3</i>	<i>Set4</i>
All _{3DGS}	26.91	25.92	53.12	61.93	82.52	61.53
All _{Scaffold GS}	28.04	26.87	51.93	58.25	78.64	57.85
E _{3DGS} + R _{3DGS}	26.86	25.93	52.90	60.38	80.49	58.14
E _{Scaffold GS} + R _{3DGS}	27.91	26.47	48.95	58.69	77.92	57.41
E _{Scaffold GS} + R _{2DGS}	28.09	26.77	48.05	56.94	75.72	55.52

Table A3: The comparison of different compound modes of Gaussians on the Waymo dataset, with each metric averaged across all clips. ALL_* delegates representing the scene with one united Gaussian. E_* and R_* separately means modeling the environment and road with a specific Gaussian method. As for the road part modeled by 3DGS or 2DGS of each mode, we impose the same SDF regularization. Note that all the implementations in the table are initialized from a point cloud with the sky sphere enabled.

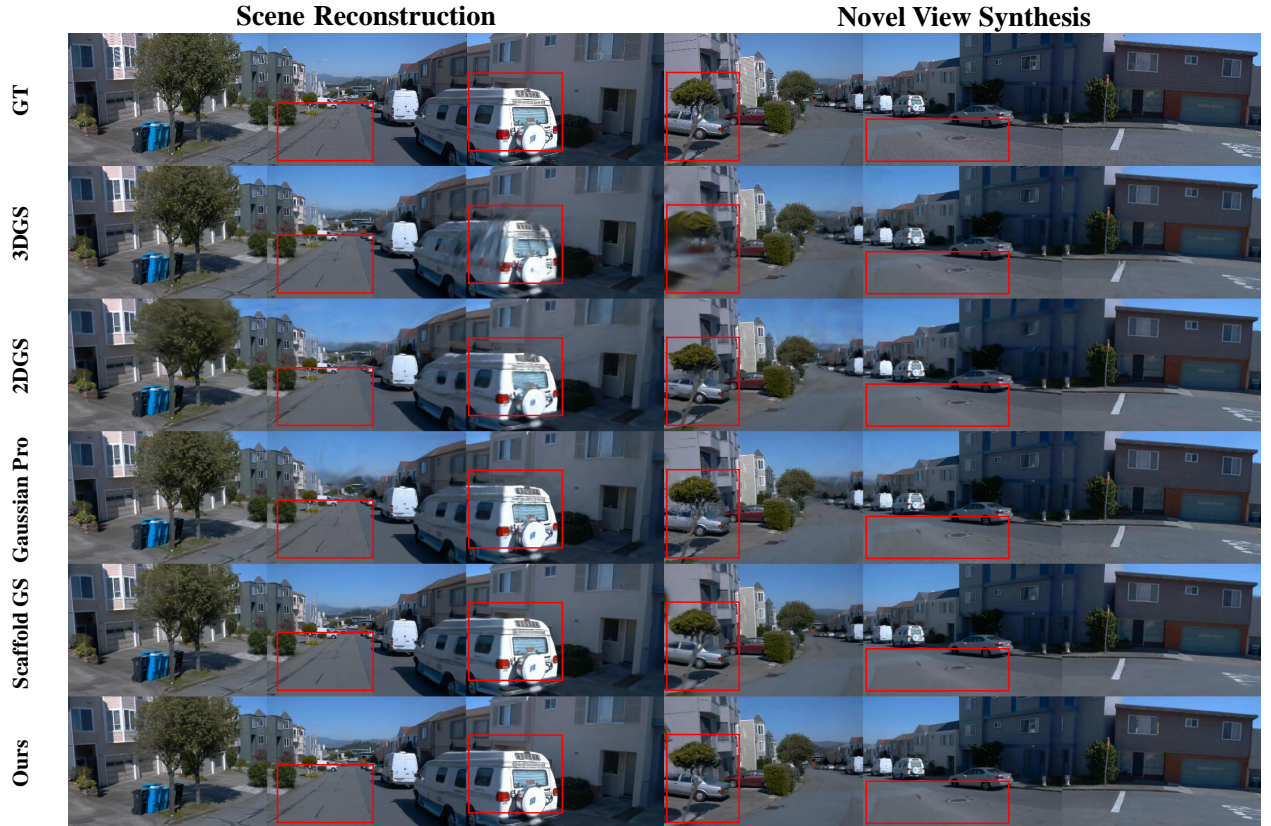


Figure A5: Qualitative comparisons on the Waymo dataset, the highlighted regions demonstrate that our method achieves the best rendering quality for both scene reconstruction in the left column and novel view synthesis in the right column.

Free-view Novel View Synthesis

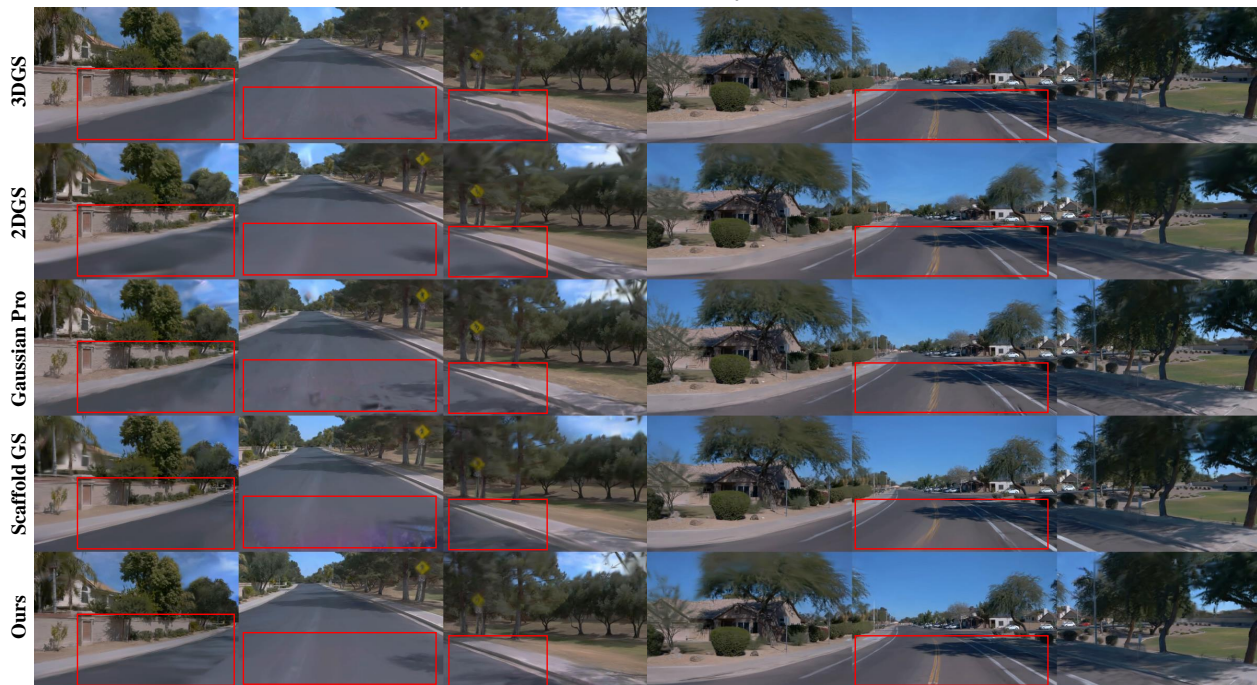


Figure A6: Qualitative results of free-view novel view synthesis under different scenarios, with the left column presenting the outputs from *Set3* and the right column showing those from *Set4*. The highlighted red boxes demonstrate that our method excels in capturing fine details both in terms of geometry and appearance.

Free-view Novel View Synthesis



Figure A7: Qualitative results of free-view novel view synthesis under different scenarios, with the left column presenting the outputs from *Set3* and the right column showing those from *Set4*. The highlighted red boxes demonstrate that our method excels in capturing fine details both in terms of geometry and appearance.